



# Superior carbon black: High-performance anode and conducting additive for rechargeable Li- and Na-ion batteries

Ki-Hun Nam<sup>a,b</sup>, Keun Hwa Chae<sup>c</sup>, Jeong-Hee Choi<sup>d</sup>, Ki-Joon Jeon<sup>e,f,\*</sup>, Cheol-Min Park<sup>a,b,\*</sup>

<sup>a</sup> School of Materials Science and Engineering, Kumoh National Institute of Technology, 61 Daehak-ro, Gumi, Gyeongbuk 39177, Republic of Korea

<sup>b</sup> Department of Energy Engineering Convergence, Kumoh National Institute of Technology, 61 Daehak-ro, Gumi, Gyeongbuk 39177, Republic of Korea

<sup>c</sup> Advanced Analysis Center, Korea Institute of Science and Technology (KIST), 14-gil 5 Hwarang-ro, Seongbuk-gu, Seoul 02792, Republic of Korea

<sup>d</sup> Next Generation Battery Research Center, Korea Electrotechnology Research Institute, 12 Jeongui-gil, Changwon, Gyeongnam 51543, Republic of Korea

<sup>e</sup> Department of Environmental Engineering, Inha University, 100 Inha-ro, Nam-gu, Incheon 22212, Republic of Korea

<sup>f</sup> Program in Environmental and Polymer Engineering, Inha University, 100 Inha-ro, Incheon 22212, Republic of Korea

## ARTICLE INFO

### Keywords:

Carbon black  
Amorphization  
Pre-lithiation/sodiation  
Li-ion batteries  
Na-ion batteries

## ABSTRACT

Carbon black (CB) is an inexpensive and widely used carbonaceous material. However, the reversibility between CB and Li or Na is very poor, and the initial coulombic efficiency (ICE) is so low that it cannot be used as an electrode material for rechargeable batteries. In this study, we successfully designed superior CB as a high-performance conducting additive for Li-ion batteries (LIBs) and Na-ion batteries (NIBs) using a simple two-step strategy: amorphization and pre-lithiation/sodiation. The Li- and Na-reversible capacities of amorphized CB increased significantly from 213 to 564 mAh g<sup>-1</sup> for LIB and from 92 to 209 mAh g<sup>-1</sup> for NIB; however, the corresponding ICEs of 61.5% for LIB and 33.5% for NIB are poor. The poor ICEs are supplemented via pre-lithiation/sodiation in the amorphized CB, which show over 100% ICEs with high Li- and Na-reversible capacities. Specifically, the modified CB has highly reversible capacities (>500 mAh g<sup>-1</sup> for LIB, >300 mAh g<sup>-1</sup> for NIB) with exceptionally high ICEs (133% ICE for LIB, 160% ICE for NIB), stable reversible capacities for over 100 cycles (470 mAh g<sup>-1</sup> for LIB, 278 mAh g<sup>-1</sup> for NIB), fast rate capabilities with highly reversible capacities at a 3C rate (~330 mAh g<sup>-1</sup> for LIB, ~190 mAh g<sup>-1</sup> for NIB), and excellent cycling behavior for over 300 cycles at a 1C rate. When used as a conducting additive, this CB contributes to high electrical conductivity and increase of ICE and the reversible capacity for LIB and NIB anode materials. These results are expected to have a significant impact on LIBs and NIBs.

## 1. Introduction

To meet the human desire for longer lasting mobile devices and electric vehicles, rechargeable batteries with better electrochemical performance have been heavily pursued. Of the various rechargeable batteries, rechargeable Li-ion batteries (LIBs) are considered to be representative secondary battery systems [1,2] and rechargeable Na-ion batteries (NIBs) are considered future alternative to LIBs [3,4]. Graphite is a representative LIB anode material because Li can intercalate into the graphene layer gaps in graphite, which contributes to excellent cycling behavior. However, graphite has a relatively small theoretical capacity (LiC<sub>6</sub>: 372 mAh g<sup>-1</sup>) and poor rate capability [5,6]. By contrast, Na ion cannot intercalate into the graphene layer gaps in graphite because of its large ionic radius. Thus, hard carbon is a promising anode for NIBs but

has a relatively small reversible capacity, low initial coulombic efficiency (ICE), and poor rate capability [7,8]. In addition to graphite and hard carbon, various carbonaceous materials, such as soft carbon, graphene, carbon nanotubes, and carbon fibers, have been widely applied to anodes for LIB and NIB systems. However, these have several disadvantageous features, such as poor ICEs, high manufacturing costs, low reversible capacities, and poor rate capabilities [9–12]. For high-capacity LIBs and NIBs, Li/Na-alloy-based and metallic Li/Na-based anodes have been extensively studied [13–17]. Of the various Li/Na-alloy-based materials, IV (Si, Ge, and Sn) and V (P, Sb, and Bi) group-based materials have been heavily investigated as high-capacity anode materials for LIBs and NIBs, respectively. However, the Li/Na-alloy-based materials undergo large volume variations during Li and Na cycling, resulting in poor Li- and Na-cycling behaviors. Metallic Li/Na-

\* Corresponding authors at: Program in Environmental and Polymer Engineering, Inha University, 100 Inha-ro, Incheon 22212, Republic of Korea (K.-J. Jeon). Department of Energy Engineering Convergence, Kumoh National Institute of Technology, 61 Daehak-ro, Gumi, Gyeongbuk 39177, Republic of Korea (C.-M. Park).  
E-mail addresses: [kjjeon@inha.ac.kr](mailto:kjjeon@inha.ac.kr) (K.-J. Jeon), [cmpark@kumoh.ac.kr](mailto:cmpark@kumoh.ac.kr) (C.-M. Park).

<https://doi.org/10.1016/j.cej.2021.129242>

Received 7 December 2020; Received in revised form 15 February 2021; Accepted 1 March 2021

Available online 10 March 2021

1385-8947/© 2021 Elsevier B.V. All rights reserved.

based anodes also have several drawbacks, such as dendrite formation and aggregation during cycling, which leads to internal short circuits of the battery cell.

Carbon black (CB) is an inexpensive and widely used carbonaceous material because it can be produced simply by the incomplete combustion of various tars or other extraneous materials [18]. In general, CB consists of tightly bonded and micron-sized chain-like clusters consisting of spherical primary particles with diameters of 10–500 nm. The sizes of the spherical primary particles affect the application properties of a product. Most CBs are used as a reinforcing filler of tires and in various rubber applications, black pigments, and other extraneous materials. In addition, it is also utilized as a conducting agent for battery electrodes due to its high electrical conductivity [19,20]. Unfortunately, despite these interesting characteristics, CB cannot be utilized as an anode material for LIBs and NIBs because it has low Li and Na reversibility, resulting in very poor ICEs and reversible capacities. Although many studies have focused on improving the electrochemical performance of CB, their ICEs and reversible capacities have been insufficient for commercialization [21–24]. Therefore, if CB with superior electrochemical performance is developed, it can be utilized as a high-performance conducting additive in rechargeable LIB and NIB systems with ripple effects in the secondary battery industry.

In this study, we suggest a new two-step strategy for developing CB for LIBs and NIBs. First, to increase the Li- and Na-reversible capacities, an increased number of Li- and Na-insertion sites were generated by preparing amorphized CB. Second, to supplement the poor ICE, the amorphized CB was pre-lithiated/sodiated, and subsequently tested as an anode material for LIBs and NIBs. In addition, the structural and bonding characteristics of CB, amorphized CB, and amorphized/pre-lithiated and -sodiated CB were investigated using various analytical techniques. In addition, the Li- and Na-insertion/extraction mechanisms of CB, amorphized CB, and amorphized/pre-lithiated and -sodiated CB were thoroughly investigated using C K-edge near edge X-ray absorption fine structure (NEXAFS).

## 2. Experimental section

### 2.1. Sample preparation

CB (Super P, Timcal Inc.) was used as a starting material. The amorphized CB was prepared using a simple high-energy milling process. The details are as follows. CB and hardened-steel balls were assembled at a powder-to-ball ratio of 1:20 wt% in a hardened steel container under an Ar-filled glove box. The assembled container was milled for 3 h using a SPEX-8000 (SPEX SamplePrep) at a motor speed of ~ 1425 RPM. Prior to synthesis to remove trapped moisture in the samples, all samples were dried at 80 °C under vacuum overnight. The amorphized/pre-lithiated and -sodiated CB was synthesized using a simple heat treatment under an Ar atmosphere. Details of the pre-lithiation/sodiation process in the amorphized CB are as follows. First, the Li/Na metal chips with amorphized CB powders were mixed using high-energy milling for 1 h. The mixture powder was then placed in a sealed quartz tube and heat-treated at 600 °C (for pre-lithiation) and 500 °C (for pre-sodiation) for 5 h at a heating rate of 5 °C min<sup>-1</sup> under an Ar atmosphere. The pre-lithiation/sodiation temperature was determined on the basis of the optimized electrochemical performance, such as ICE and reversible capacity of the amorphized/pre-lithiated and -sodiated CB electrodes.

### 2.2. Material characterization

An X-ray diffraction (XRD) measurement was conducted using a Rigaku MiniFlex 600 with a Cu target. For air-sensitive materials (amorphized/pre-lithiated and -sodiated CB), the samples were laminated using Kapton tape before XRD measurement. The Fourier-transform infrared (FT-IR, Vertex 80v, Bruker Inc.) spectra on a KBr

pellet were recorded at 4000–500 cm<sup>-1</sup>. The Raman spectra were recorded using a System 1000 spectrometer (Renishaw Inc.) at 2000–100 cm<sup>-1</sup> under intense excitation of a 514-nm laser. The Brunauer-Emmett-Teller (BET)/Barrett-Joyner-Halenda (BJH) measurements were analyzed on a 3-Flex (Micromeritics Inc.) to characterize the specific surface area and pore size. The morphological and structural characteristics of materials were identified through scanning electron microscopy (SEM) using a MAIA 3 LM (TESCAN Inc.) at an acceleration voltage of 30 kV and through a Cs-corrected high resolution transmission electron microscopy (TEM) using a JEM-ARM200F (JEOL Inc.) at an acceleration voltage of 200 keV, respectively. Energy-loss spectra were acquired using an electron energy loss spectroscopy (EELS, Model 965 GIF Quantum ER) attached to TEM, and the energy resolution of the EELS was ~ 0.5 eV as measured by the full width at half-maximum of the zero-loss peak. The scanning TEM (STEM) image with corresponding EELS elemental maps was recorded at 40 × 40 pixels. The energy ranges of the EELS were 55–85 eV, 1060–1200 eV, and 270–360 eV for the Li-, Na-, and C-K-edges, respectively. The C K-edge NEXAFS spectra were recorded at beamline 10D (XAS-KIST) at the Pohang Accelerator Laboratory (PAL) in South Korea. The NEXAFS spectra were obtained in the energy range of 280–310 eV at total electron yield (TEY) mode under the pressure of ~ 1.5 × 10<sup>-8</sup> Torr at an energy resolution of 0.6 eV.

### 2.3. Electrochemical measurement

All active materials (CB, amorphized CB, and amorphized/pre-lithiated and -sodiated CB) and polyvinylidene fluoride (PVDF) binder were dried overnight at 80 °C under vacuum conditions to remove O<sub>2</sub> and H<sub>2</sub>O. The CB, amorphized CB, graphite, and hard carbon electrodes were fabricated using a conventional slurry coating method. The slurry consisted of active material, a conducting carbon agent, and a PVDF binder at a ratio of 80:10:10 wt% dissolved in a N-methyl-2-pyrrolidone (NMP) solvent, then casted on Cu foil (thickness: 11 μm) using a doctor blade. The electrode fabrication of amorphized/pre-lithiated and -sodiated CB was handled in an Ar-filled glove box because the samples are air-sensitive. Amorphized/pre-lithiated and -sodiated CB electrode was prepared through a slurry consisting of active material, a conducting carbon agent, and PVDF at a ratio of 80:10:10 wt%, dissolved in a 1,3-dioxolane solvent. Each slurry was cast on Cu foil in an Ar-filled glove box and dried under vacuum. All coin-type half cells were assembled in an Ar-filled glove box using Li/Na foil as the counter and reference electrodes, electrolyte (1 M LiPF<sub>6</sub> in ethylene carbonate (EC): diethyl carbonate (DEC, 1:1 v/v) for LIB, 1 M NaClO<sub>4</sub> in EC:DEC (1:1 v/v) for NIB), and separator (Celgard 2400 for LIB, Whatman glass fibre-D for NIB). The electrochemical impedance spectroscopy (EIS) of the assembled cells for LIBs and NIBs was performed with ZIVE-MP2A (ZIVE LAB) at frequencies of 100 kHz to 10 mHz. All battery performances were analyzed using a Maccor-4000 series battery cyclor tester.

## 3. Results and discussion

### 3.1. Carbon black and its amorphization

Fig. 1a–b and Figure S1a–b show the voltage profiles and cycling performances of CB as LIB and NIB anodes. The first Li- and Na-insertion/extraction capacities for LIB and NIB were 441/213 and 428/92 mAh g<sup>-1</sup>, respectively. Although the Li- and Na-cycling performances of CB were stable (Figures S1a and S1b), it had very poor corresponding ICEs (48.3% for LIB, 21.5% for NIB) and low reversible capacities (~200 mAh g<sup>-1</sup> for LIB, ~90 mAh g<sup>-1</sup> for NIB), demonstrating that CB cannot be used as anode materials for LIBs and NIBs. The poor reversibility and ICEs of CB were originated from the formation of solid electrolyte interface layer and the various chemisorbed species of hydroxyl (–OH), carbonyl (–C=O), carboxyl (–COOH), etc., on carbons during the manufacturing process [25–27], which was confirmed by FT-

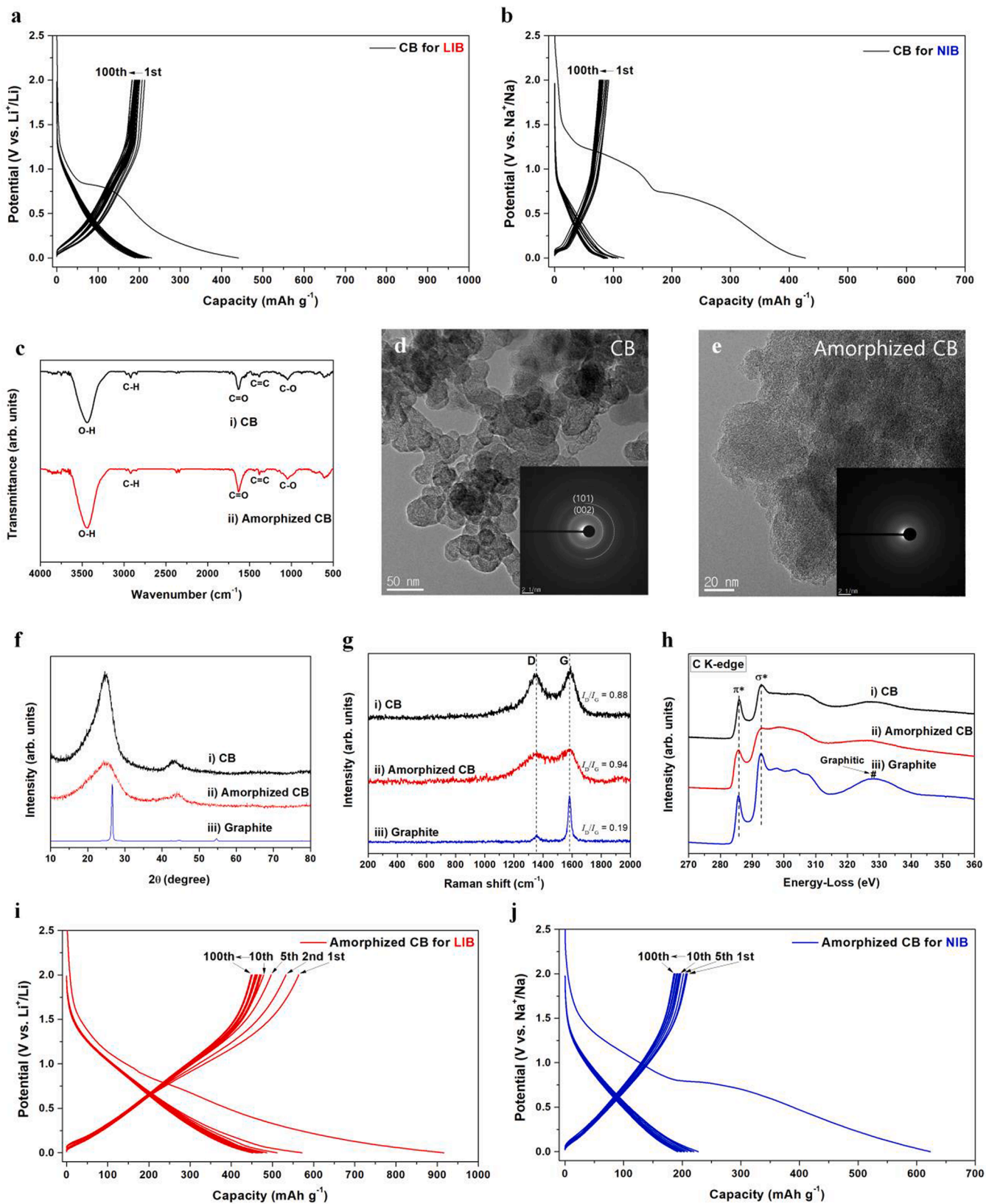


**Fig. 1. Characteristics of CB and amorphized CB.** (a) Voltage profiles of CB as a LIB anode (current density:  $100 \text{ mA g}^{-1}$ ). (b) Voltage profiles of CB as a NIB anode (current density:  $50 \text{ mA g}^{-1}$ ). (c) IR spectra of CB and amorphized CB. (d) BF-TEM image of CB and its corresponding DPs. (e) BF-TEM image of amorphized CB and its corresponding DPs. (f) XRD results of CB, amorphized CB, and graphite. (g) Raman spectra of CB, amorphized CB, and graphite. (h) EELS spectra of CB, amorphized CB, and graphite. (i) Voltage profiles of amorphized CB as a LIB anode (current density:  $100 \text{ mA g}^{-1}$ ). (j) Voltage profiles of amorphized CB as a NIB anode (current density:  $50 \text{ mA g}^{-1}$ ).

IR spectroscopy results of CB, as shown in Fig. 1c-i. During Li/Na insertion, the chemisorbed species generated various Li/Na-irreversible phases, resulting in poor electrochemical performances. In addition, to analyze the morphological and structural characteristics of CB, SEM, TEM, XRD, Raman spectroscopy, and C K-edge EELS analyses were performed, and the results are shown in Figure S2 and Fig. 1d, 1f, 1g, and 1h, respectively. The SEM images in Figure S2a-b show that CB was composed of chain-like clusters consisting of approximately 30–50-nm-sized spherical primary particles. In addition, the bright field (BF)-TEM image shows spherical particles, which exhibited corresponding selected area diffraction patterns (SADPs) of very dim rings of (0 0 2) and (1 0 1) planes (Fig. 1d) [28]. In addition, the XRD pattern of CB also showed very broad peaks of main (0 0 2) and (1 0 1) planes (Fig. 1f-i) compared to those of graphite (Fig. 1f-iii). In Fig. 1g-i and -iii, the Raman spectrum of CB exhibited two peaks of  $1355\text{ cm}^{-1}$  (D band) and  $1580\text{ cm}^{-1}$  (G band), which is consistent with those of graphite. However, CB had significantly reduced Raman peaks and a very low intensity ratio of  $I_D/I_G$  compared to that of graphite. The EELS spectrum of CB confirmed the presence of peaks of  $\pi\text{-}\pi^*$  ( $\pi^*$ ,  $\sim 286\text{ eV}$ ) and  $\sigma\text{-}\sigma^*$  ( $\sigma^*$ ,  $\sim 293\text{ eV}$ ) bonds as well as a graphitic peak ( $\#$ ,  $\sim 330\text{ eV}$ ), as shown in Fig. 1h-i [29–31]. However, the  $\sigma^*$  peak intensity was relatively low compared to that of graphite (Fig. 1h-iii). In addition, the EELS graphitic peak ( $\sim 330\text{ eV}$ ) of CB was smaller and wider than that of graphite. Therefore, the results of TEM, XRD, Raman, and C K-edge EELS analyses demonstrate that CB has a nearly amorphous structure with partially developed distorted layers.

To endow more Li- and Na-insertion sites in CB, a high-energy milling process was performed on CB to produce more amorphized CB. In general, high-energy milling generates high pressure ( $\sim 6\text{ GPa}$ ) and temperature ( $\sim 200\text{ }^\circ\text{C}$ ) during the process, and the conditions are sufficient to convert crystalline materials into amorphous or reduced crystalline materials [32,33]. The morphological and structural characteristics of high-energy milling-treated CB were also analyzed using SEM, TEM, XRD, Raman, and C K-edge EELS. The SEM and BF-TEM images of high-energy milling-treated CB confirmed that it consisted of broken and agglomerated amorphous C clusters (Figure S2c-d and Fig. 1e). Interestingly, the SADPs did not show any ring patterns (Fig. 1e), which also confirmed the amorphization of CB. The XRD results of high-energy milling-treated CB showed the reduced crystallinity, resulting in a decrease in peak intensity and a slight peak shift (Fig. 1f-ii). The Raman spectrum of high-energy milling-treated CB also showed reduced peak intensity (Fig. 1g-ii). In addition, the  $I_D/I_G$  in Raman spectrum of high-energy milling-treated CB was higher ( $\sim 0.94$ ) than that of CB ( $\sim 0.88$ ), which was caused by the increased defects during high-energy milling. Therefore, increased defects of high-energy milling-treated CB can provide large Li- and Na-insertion sites, facilitating enhancement of the electrochemical performance. The C K-edge EELS spectrum of high-energy milling-treated CB was also analyzed. The C K-edge EELS peak shapes of  $\pi^*$  and  $\sigma^*$  bonds were more broadened (Fig. 1h-ii). In addition, the EELS graphitic peak ( $\#$ ,  $\sim 330\text{ eV}$ ) of high-energy milling-treated CB nearly disappeared [31]. Furthermore, results of BET/BJH analyses showed that the specific surface area and pore volume distribution of high-energy milling-treated CB were  $186.7\text{ m}^2\text{ g}^{-1}$  and  $3.8\text{ nm}$  (Figure S3b), respectively, the values of which increased significantly as compared to those of the corresponding values of CB ( $64\text{ m}^2\text{ g}^{-1}$  and  $2.5\text{ nm}$ , Figure S3a). Consequently, these SEM, TEM, XRD, Raman, C K-edge EELS, and BET/BJH analytical results demonstrate that the structure of CB was transformed into fully amorphized CB through a facile high-energy milling process.

The amorphized CB showed much higher first discharge/charge capacities of  $916/564\text{ mAh g}^{-1}$  for LIB (Fig. 1i) and  $623/209\text{ mAh g}^{-1}$  for NIB (Fig. 1j) than CB. This was attributed to the generation of an increased number of Li- and Na-insertion sites and high surface area/pore volume distribution through the amorphization of CB. The Li- and Na-reversible capacities were stabilized after the 10th cycle with  $479$  and  $202\text{ mAh g}^{-1}$  for LIB and NIB, respectively, and they were well retained even after the 100th cycle with  $93.7\%$  and  $92.6\%$  for LIB and

NIB capacity retentions, respectively. Despite the high reversible capacities and cycling performances of amorphized CB, results still showed poor ICEs of  $61.5\%$  for LIB and  $33.5\%$  for NIB with increased irreversible capacities compared to those of CB, which was originated from the increased formation of irreversible solid electrolyte interface layers by the increased surface area/pore volume distribution through the amorphization of CB. FT-IR results of amorphized CB were nearly identical to those for CB (Fig. 1c-ii), confirming that the various chemisorbed species on carbons did not vary by the high-energy milling process, which also affected the poor ICEs. For application of amorphized CB to practical LIB and NIB systems, the poor ICEs must be supplemented. In addition, to compare the electrochemical reaction resistances of CB, amorphized CB, and commercial carbon-based (graphite for LIB, hard carbon for NIB) electrodes, their EIS results were compared (Figure S4). The CB and amorphized CB electrodes had similar semicircles in LIB (Figure S4a) and NIB (Figure S4c) systems and much smaller semicircles than those of commercial graphite in LIB or hard carbon in NIB. This confirmed that CB and amorphized CB in both LIB and NIB systems have better electrochemical conductivity than graphite in LIB or hard carbon in NIB. The good electrochemical conductivity of CB and amorphized CB originated from the intrinsic characteristics of conducting CB [18,34]. In addition, the plots of impedance ( $Z_{re}$ ) vs. inverse square root of angular frequency ( $\omega^{-1/2}$ ) are shown in Figures S4b for LIB and S4d for NIB, and the fitted slopes are the Warburg constant ( $\sigma$ ) for each sample. CB and amorphized CB had similar calculated Li-ion diffusion coefficients (CB:  $5.21 \times 10^{-17}\text{ cm}^2\text{ s}^{-1}$ ; amorphized CB:  $2.16 \times 10^{-17}\text{ cm}^2\text{ s}^{-1}$ ) in the LIB system and Na-ion diffusion coefficients (CB:  $7.16 \times 10^{-18}\text{ cm}^2\text{ s}^{-1}$ ; amorphized CB:  $4.37 \times 10^{-17}\text{ cm}^2\text{ s}^{-1}$ ) in the NIB system, which were higher than those of commercial graphite in LIB ( $6.48 \times 10^{-18}\text{ cm}^2\text{ s}^{-1}$ ) or hard carbon in NIB ( $8.14 \times 10^{-19}\text{ cm}^2\text{ s}^{-1}$ ).

### 3.2. Pre-lithiation/sodiation of amorphized carbon black

Recently, the use of pre-lithiated/sodiated materials has been suggested as an alternative strategy to improve the ICEs of LIB and NIB electrodes. However, the pre-lithiated/sodiated materials were processed using difficult and complicated methods, such as chemical treatment using active reactants, electrochemical pre-lithiation/sodiation, and direct contact with Li/Na metal powders [35–40]. Although the suggested approaches for pre-lithiation/sodiation showed an enhanced ICE, their difficult and complicated synthesis processes and the high reactivity of pre-lithiated/sodiated materials hinder commercialization. Therefore, we newly developed a simple pre-lithiation/sodiation processing method to enhance the poor ICEs of amorphized CB. Considering the first irreversible capacities of amorphized CB,  $0.3\text{ mol Li/Na}$  was pre-lithiated/sodiated in the amorphized CB. Additionally, the amount of pre-lithiation/sodiation can be controlled easily on the basis of the operating voltage of half/full cells. The pre-lithiation/sodiation process involves a simple heat-treatment ( $600\text{ }^\circ\text{C}$  for pre-lithiation,  $500\text{ }^\circ\text{C}$  for pre-sodiation) after mixing of Li/Na metal chips with amorphized CB powders using high-energy milling for 1 h. The sequential amorphization and pre-lithiation/sodiation processes are schematically shown in Fig. 2a. First, to increase the reversible capacity of CB, an increased number of Li- and Na-insertion sites were generated by its amorphization. Second, pre-lithiation/sodiation in amorphized CB was processed to supplement its poor ICEs. To confirm the pre-lithiation/sodiation in amorphized CB, the as-synthesized amorphized/pre-lithiated and -sodiated CB was analyzed using various analytical tools, such as XRD, Raman, TEM, and Li/Na K-edge and C K-edge EELS. However, XRD patterns of the amorphized/pre-lithiated and -sodiated CB did not change and still had amorphous characteristics, as shown in Figures S5a (for LIB) and S5b (for NIB). Raman spectra of amorphized/pre-lithiated and -sodiated CB are also shown in Figures S6a (for LIB) and S6b (for NIB), and the Raman peak at  $1580\text{ cm}^{-1}$  (G band) shifted to the left as compared to that of the amorphized

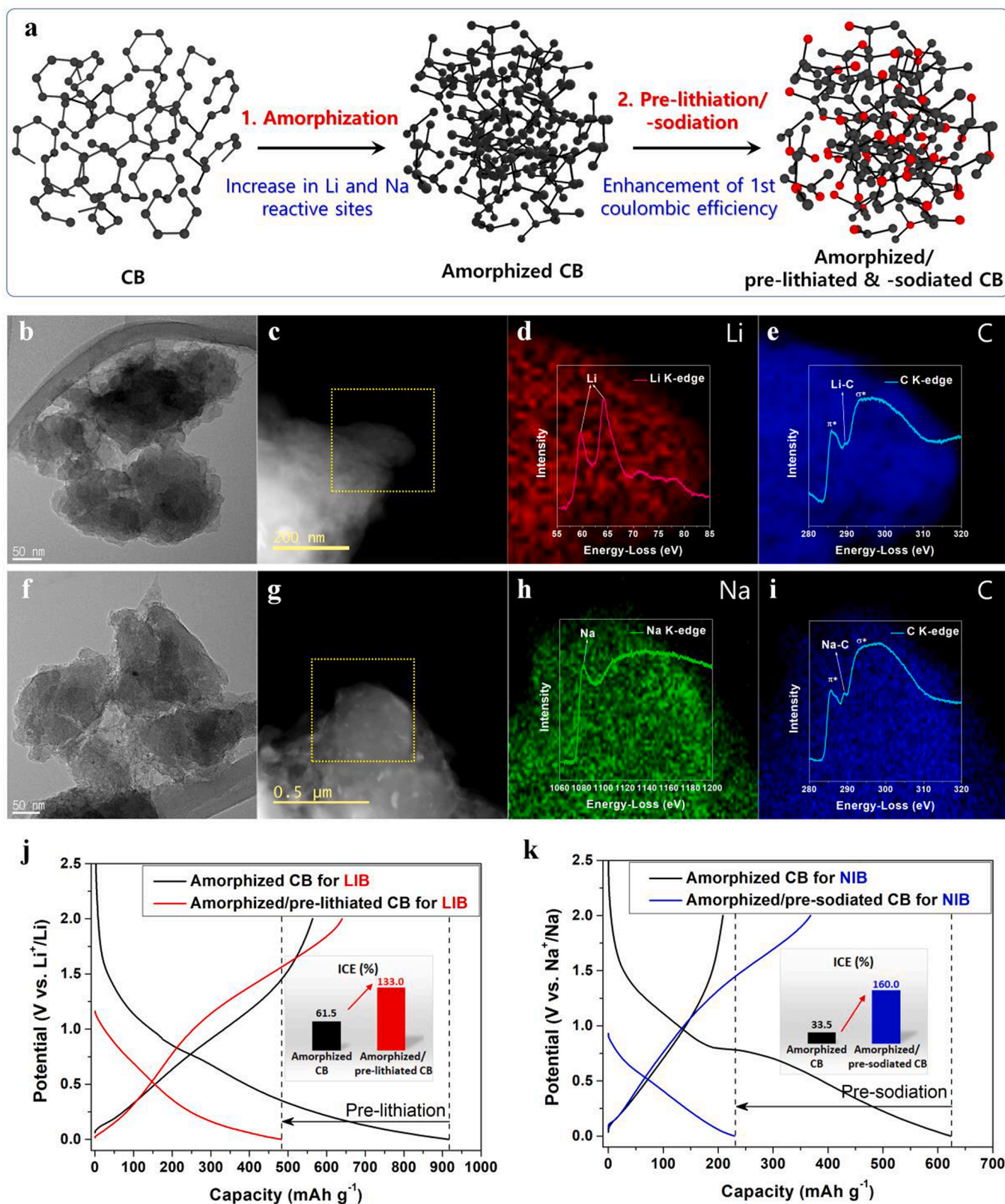


**Fig. 2.** Synthesis and characteristics of amorphized/pre-lithiated and -sodiated CB. (a) Schematic representation of a simple two-step process of amorphization and pre-lithiation/-sodiation. (b) BF-TEM of amorphized/pre-lithiated CB. (c) STEM of amorphized/pre-lithiated CB. (d) EELS elemental Li maps (red) and corresponding Li EELS spectrum. (e) EELS elemental C maps (blue) and corresponding C EELS spectrum with Li-C bond. (f) BF-TEM of amorphized/pre-sodiated CB. (g) STEM of amorphized/pre-sodiated CB. (h) EELS elemental Na maps (green) and corresponding Na EELS spectrum. (i) EELS elemental C maps (blue) and corresponding C EELS spectrum with Na-C bond. (j) Voltage profiles of amorphized CB and amorphized/pre-lithiated CB for LIB anodes (current density:  $100 \text{ mA g}^{-1}$ ). (k) Voltage profiles of amorphized CB and amorphized/pre-sodiated CB for NIB anodes (current density:  $50 \text{ mA g}^{-1}$ ).

CB and, thus, were broadened into one peak [41]. The BF-TEM images of the amorphized/pre-lithiated and -sodiated CB confirm that they had broken and agglomerated amorphous C clusters, which is similar to amorphized CB, as shown in Fig. 2b (amorphized/pre-lithiated CB) and 2f (amorphized/pre-sodiated CB). In general, elemental mapping of Li and Na using energy dispersive X-ray spectroscopy is difficult because Li and Na are too light and have low energy domains. Therefore, to examine the compositional properties of the amorphized/pre-lithiated and -sodiated CB in detail, EELS analyses combined with TEM were conducted. The EELS elemental maps clearly demonstrate that elemental Li (Fig. 2d) and Na (Fig. 2h) were dispersed uniformly within the amorphous carbon (Fig. 2e and 2i). The corresponding Li/Na K-edge and C K-edge EELS spectra for the amorphized/pre-lithiated and -sodiated CB are also shown in the insets in the EELS elemental maps. The EELS spectra clearly demonstrate the effective dispersion of Li and Na in amorphous carbon with the corresponding absorption edges of Li ( $\sim 60$  and  $\sim 65$  eV, Fig. 2d) and Na ( $\sim 1082$  eV, Fig. 2h) [42]. In addition, the C K-edge EELS peaks of  $\pi^*$  and  $\sigma^*$  bonds were nearly the same as those of the amorphized CB (Fig. 2e and 2i). Interestingly, a tiny C K-edge EELS peak at  $\sim 289$  eV was newly developed, which could be related to Li-C and Na-C bonds. The electrochemical performances of amorphized/pre-lithiated and -sodiated CB were tested galvanostatically, and their first cycle voltage profiles are shown in Fig. 2j and 2k, respectively. Interestingly, the open circuit voltages (OCVs) of amorphized/pre-lithiated and -sodiated CB were 1.16 V and 0.93 V, respectively, which also demonstrates the effective formation of amorphized/pre-lithiated and -sodiated CB. The first Li-insertion/extraction capacity of amorphized/pre-lithiated CB was 482/640 mAh  $g^{-1}$  with an exceptionally high ICE of 133%. In addition, the Na-insertion/extraction capacity of amorphized/pre-sodiated CB showed 230/368 mAh  $g^{-1}$  with an exceptionally high ICE of 160%. Although the operating voltage was relatively higher than those of commercial graphite and hard carbon anodes, the cell potential can be selected by use of the amount of amorphized/pre-lithiated and -sodiated CB on the basis of the operating voltage of full cell. The results of EELS and electrochemical performances demonstrate that the amorphized/pre-lithiated and -sodiated CB was synthesized successfully and exhibited exceptionally high ICEs of over 100% with a high first Li/Na-extraction capacity.

### 3.3. Li- and Na-insertion/extraction mechanisms of amorphized/pre-lithiated and -sodiated carbon black

To understand the Li- and Na-insertion/extraction mechanisms of CB, amorphized CB, and amorphized/pre-lithiated and -sodiated CB, C K-edge NEXAFS analyses were performed with the results shown in Fig. 3. Fig. 3a-i and 3b-i show that the main C K-edge NEXAFS absorption energy of CB was involved at  $\sim 286$  eV ( $\pi^*$ ) and  $\sim 293$  eV ( $\sigma^*$ ) [43], the values for which coincided with those of C K-edge EELS results presented in Fig. 1h, 2e, and 2i. At the full Li/Na-insertion states (0 V, Fig. 3a-ii and 3b-ii), new absorption peaks at  $\sim 288.7$  eV (denoted as peak A) and  $\sim 290.3$  eV (denoted as peak B) were developed. However, at the full Li/Na-extraction states (2 V, Fig. 3a-iii and 3b-iii), peak A remained unchanged, whereas the intensity of peak B diminished. These C K-edge NEXAFS results of CB demonstrate that peaks A and B are related to the irreversible and reversible Li-C/Na-C reactions, respectively (Fig. 3c). In Fig. 3d-i and 3e-i, amorphized CB had C K-edge NEXAFS peaks similar to those of CB. However, at the full Li/Na-insertion states (0 V, Fig. 3d-ii and 3e-ii), peaks A and B were developed in a similar manner to CB, but the intensity of peak B for amorphized CB was higher than that of CB, which is related to the higher Li/Na-insertion capacity of amorphized CB than that of CB. Interestingly, at the full Li/Na-extraction states (2 V, Fig. 3d-iii and 3e-iii), the large peak B nearly disappeared; whereas, peak A remained unchanged, thus further demonstrating that peak A is related to the irreversible Li-C/Na-C reaction. The C K-edge NEXAFS results of amorphized CB efficiently explain its higher Li- and Na-insertion/extraction capacities than

those of CB (Fig. 3f). Interestingly, for amorphized/pre-lithiated and -sodiated CB, the main absorption energy ( $\pi^*$  and  $\sigma^*$ ) of CB was not nearly generated. Instead, only the irreversible peak A developed (Fig. 3g-i and 3 h-i), which demonstrates that the amorphized/pre-lithiated and -sodiated CB was successfully synthesized and the majority of the amorphized/pre-lithiated and -sodiated contributed to the formation of irreversible Li-C/Na-C. In addition, the value of the irreversible peak A coincided with those of C K-edge EELS spectrum (Fig. 2e and i). At the full Li/Na-insertion states (0 V, Fig. 3g-ii and 3 h-ii), the irreversible peak A did not change, and the reversible peak B was developed; whereas, the reversible peak B fully disappeared, and the irreversible peak A remained unchanged at the full Li/Na-extraction states (2 V, Fig. 3g-iii and 3 h-iii). The C K-edge NEXAFS results of amorphized/pre-lithiated and -sodiated CB show its higher Li- and Na-insertion/extraction capacities and superior reversibility with high ICE (Fig. 3i) than those of CB (Fig. 3c) and amorphized CB, which is schematically represented in Fig. 3f.

### 3.4. Superior electrochemical performances of amorphized/pre-lithiated and -sodiated carbon black

To compare the electrochemical performances of amorphized/pre-lithiated and -sodiated CB, its electrochemical voltage profiles for LIBs and NIBs are shown in Fig. 4a and 4d, respectively. The amorphized/pre-lithiated CB showed a high first Li-insertion/extraction capacity of 482/640 mAh  $g^{-1}$  with 133% ICE and 1.16 V OCV (Fig. 4a). The reversible Li-insertion capacity was stabilized after the 10th cycle with 525 mAh  $g^{-1}$ , and it was well retained even after the 100th cycle with a 91.8% capacity retention. Notably, the amorphized/pre-lithiated CB showed a stable cycling behavior with a higher ICE and reversible capacity (470 mAh  $g^{-1}$  at the 100th cycle) than those of the commercial LIB graphite anode (Fig. 4b). In addition, the amorphized/pre-lithiated CB showed a fast rate capability with highly reversible capacities at various C rates (1C:  $\sim 410$  mAh  $g^{-1}$ , 2C:  $\sim 360$  mAh  $g^{-1}$ , and 3C:  $\sim 330$  mAh  $g^{-1}$ ), which was far superior to those of commercial LIB graphite anode (Fig. 4c and S7a). Furthermore, the amorphized/pre-lithiated CB showed excellent cycling behavior during 300 cycles at a 1C rate. On the other hand, the amorphized/pre-sodiated CB showed a high first Na-insertion/extraction capacity of 230/368 mAh  $g^{-1}$  with 160% ICE and 0.93 V OCV (Fig. 4d). The reversible Na-insertion capacity was also stabilized after the 10th cycle with 321 mAh  $g^{-1}$ , and it was well retained even after the 100th cycle with 87.5% capacity retention. Notably, the amorphized/pre-sodiated CB showed a stable cycling behavior with a higher ICE and reversible capacity (280 mAh  $g^{-1}$  at the 100th cycle) than those of representative hard carbon anodes for NIBs (Fig. 4e). Furthermore, the amorphized/pre-sodiated CB showed a fast rate capability with highly reversible capacities at various C rates (1C:  $\sim 250$  mAh  $g^{-1}$ , 2C:  $\sim 200$  mAh  $g^{-1}$ , and 3C:  $\sim 190$  mAh  $g^{-1}$ ), which was far superior to those of the hard carbon anode (Fig. 4f and S7b). Moreover, the amorphized/pre-sodiated CB also showed an excellent cycling behavior during 300 cycles at a 1C rate. The fast rate capability of amorphized/pre-lithiated and -sodiated CB was attributed to the high electrochemical reaction conductivity and Li/Na-ion diffusion coefficient that originated from the intrinsic characteristics of conducting CB, which enables Li- and Na-ions to diffuse quickly within the amorphized/pre-lithiated and -sodiated CB. Further, the pre-lithiated/sodiated Li/Na in the amorphized/pre-lithiated and -sodiated CB also contributed to the fast rate capability.

### 3.5. Superior carbon black as a conducting additive for high-performance LIBs and NIBs

Owing to its superior electrochemical performances of high ICE and reversible capacity, the amorphized/pre-lithiated and -sodiated CB, designed using a simple two-step strategy of amorphization and pre-lithiation/sodiation, can be utilized as a high-performance conducting

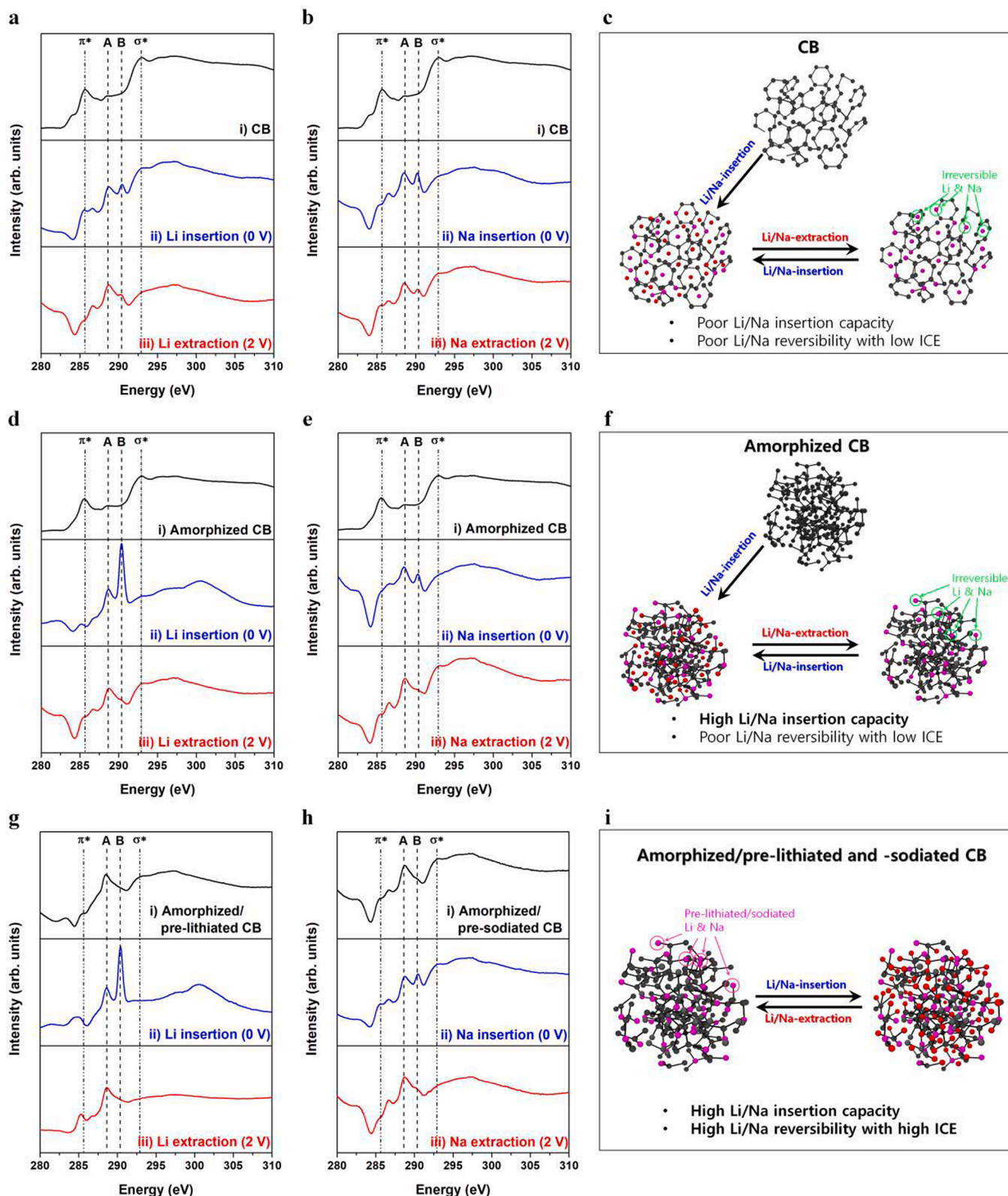


**Fig. 3.** Reaction mechanism of CB, amorphized CB, and amorphized/pre-lithiated and -sodiated CB during Li and Na reactions. (a) C K-edge NEXAFS spectra of CB for LIB anodes during the 1st Li insertion/extraction. (b) C K-edge NEXAFS spectra of CB for NIB anodes during the 1st Na insertion/extraction. (c) Schematic representation of the reaction mechanism of CB for LIBs and NIBs. (d) C K-edge NEXAFS spectra of amorphized CB for LIB anodes during the 1st Li insertion/extraction. (e) C K-edge NEXAFS spectra of amorphized CB for NIB anodes during the 1st Na insertion/extraction. (f) Schematic representation of the reaction mechanism of amorphized CB for LIBs and NIBs. (g) C K-edge NEXAFS spectra of amorphized/pre-lithiated CB for LIB anodes during the 1st Li insertion/extraction. (h) C K-edge NEXAFS spectra of amorphized/pre-sodiated CB for NIB anodes during the 1st Na insertion/extraction. (i) Schematic representation of the reaction mechanism of amorphized/pre-lithiated and -sodiated CB for LIBs and NIBs.

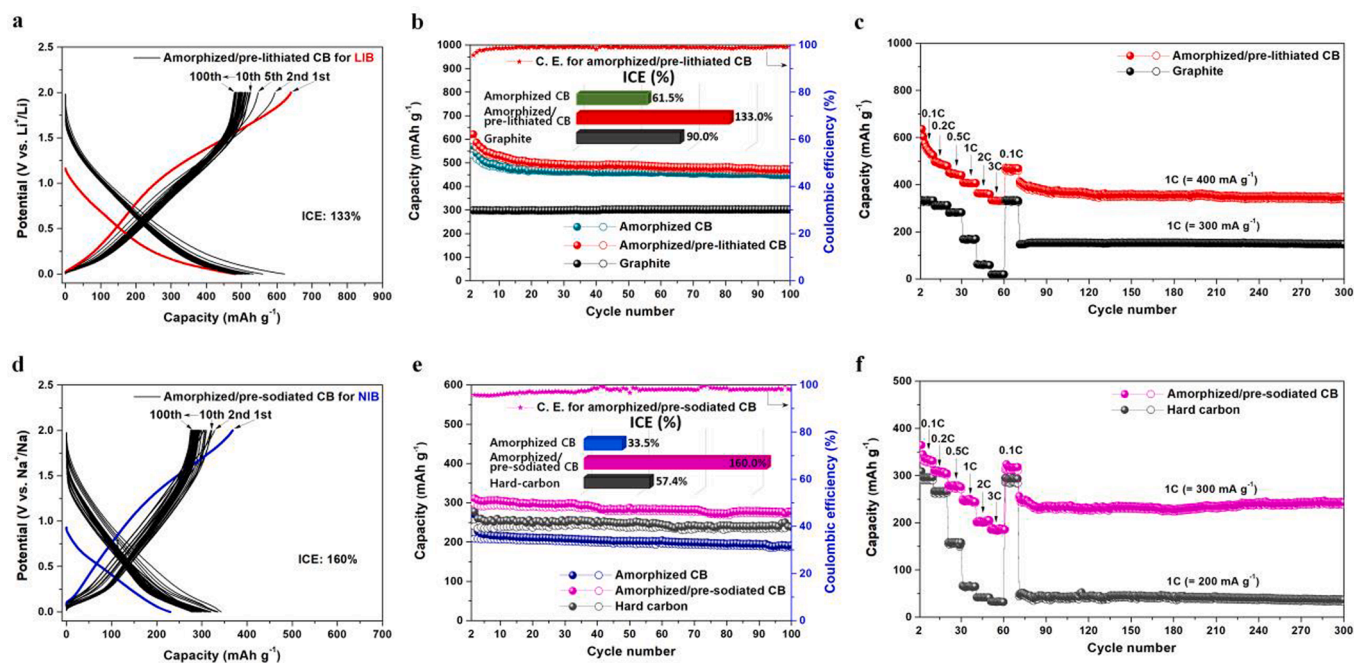


**Fig. 4.** Electrochemical performances of the amorphized/pre-lithiated and -sodiated CB. (a) Voltage profiles of amorphized/pre-lithiated CB as a LIB anode (current density:  $100 \text{ mA g}^{-1}$ ). (b) Cycling performances of amorphized CB, amorphized/pre-lithiated CB, and commercial MCMC-graphite for LIB anodes (cycling rate:  $100 \text{ mA g}^{-1}$ ). (c) Rate capabilities of amorphized/pre-lithiated CB (1C rate:  $400 \text{ mA g}^{-1}$ ) and MCMC-graphite (1C rate:  $300 \text{ mA g}^{-1}$ ) for LIB anodes. (d) Voltage profiles of amorphized/pre-sodiated CB as a NIB anode (current density:  $50 \text{ mA g}^{-1}$ ). (e) Cycling performances of amorphized CB, amorphized/pre-sodiated CB, and hard carbon for NIB anodes (cycling rate:  $50 \text{ mA g}^{-1}$ ). (f) Rate capabilities of amorphized/pre-sodiated CB (1C rate:  $300 \text{ mA g}^{-1}$ ) and hard carbon (1C rate:  $200 \text{ mA g}^{-1}$ ) for NIB anodes.

additive for LIBs and NIBs. Therefore, to compare the electrochemical performance with or without the amorphized/pre-lithiated and -sodiated CB as a conducting additive, the electrochemical performances of representative carbon-based anode materials of graphite (for LIBs) and hard carbon (for NIBs) are compared in Fig. 5a and b. The graphite anode, which consisted of graphite (80 wt%), binder (10 wt%), and conventional CB conducting agent (10 wt%), showed the first Li-insertion/extraction capacity of  $329/296 \text{ mAh g}^{-1}$  with 90% ICE and 2.8 V OCV (Fig. 5a-i). Interestingly, the graphite electrodes with the various compositions of amorphized/pre-lithiated CB conducting additive from 10 wt% to 30 wt% showed that the ICEs were increased from 94.2% to 106.3% and OCVs were decreased from 1.6 V to 1.0 V (Fig. 5a-ii-iv). The hard carbon anode, which consisted of hard carbon (80 wt%), binder (10 wt%), and conventional CB conducting agent (10 wt%), showed the first Na-insertion/extraction capacity of  $416/239 \text{ mAh g}^{-1}$  with a poor 57.4% ICE and 2.5 V OCV (Fig. 5b-i). The hard carbon electrodes with the various compositions of amorphized/pre-sodiated CB conducting additive from 10 wt% to 30 wt% also showed that the ICEs were increased from 65.7% to 80.6% and the OCVs were decreased from 1.4 V to 1.0 V (Fig. 5b-ii-iv). In addition, the electrochemical performance of graphite and hard carbon electrodes with the same composition of conventional CB conducting agent (30 wt%) and amorphized/pre-lithiated and -sodiated CB (30 wt%) is compared in Figure S8. The reversible capacities and ICEs of graphite and hard carbon containing amorphized/pre-lithiated and -sodiated CB (30 wt%) were much higher than those containing conventional CB conducting agent (30 wt%). The electrochemical performances of graphite (for LIBs, Fig. 5c-e) and hard carbon (for NIBs, Fig. 5f-h) containing the conducting additive of amorphized/pre-lithiated and -sodiated CB (30 wt%) are compared. The voltage profile and cycling performance of graphite anode containing the conducting additive of amorphized/pre-lithiated CB (30 wt%) showed an exceptionally high ICE of 106.3% with a high Li reversible capacity and exceptionally high 97.7% capacity retention from 2 to 100 cycles, which is much higher than those of the graphite

anode containing conventional CB conducting agent (Fig. 5c and d). In addition, the graphite anode containing conducting additive of amorphized/pre-lithiated CB showed a faster rate capability with highly reversible capacities at various C rates than that of the graphite anode containing conventional CB conducting agent (Fig. 5e). On the other hand, the voltage profile and cycling performance of hard carbon anode containing the conducting additive of amorphized/pre-sodiated CB (30 wt%) also showed a high ICE of 80.6% with a high Na reversible capacity and a high 99.8% capacity retention after 100 cycles, which is much higher than those of the hard carbon anode containing conventional CB conducting agent (Fig. 5f and g). In addition, the hard carbon anode containing conducting additive of amorphized/pre-sodiated CB showed a faster rate capability with highly reversible capacities at various C rates than that of the hard carbon anode containing conventional CB conducting agent (Fig. 5h). Additionally, the conducting additive of amorphized/pre-lithiated and -sodiated CB was applied to the Li- and Na-alloy-based composite anode materials of Sn/C and Sb/C for LIBs (Figures S9a and b) and for NIBs (Figures S9c and d). The poor ICEs of Sn/C and Sb/C composite anodes containing conventional CB conducting agent (10 wt% and 30 wt%) were increased significantly compared to those of the Sn/C and Sb/C composite anodes containing the conducting additive of amorphized/pre-lithiated and -sodiated CB (30 wt%). It is noteworthy that these superior electrochemical performances demonstrate that the superior conducting additive, designed using a simple two-step strategy of amorphization and pre-lithiation/sodiation, is very suitable as a next generation conducting agent to replace the conventional CB because it provides high electrical conductivity, compensates ICE, and increases the reversible capacity.

#### 4. Conclusion

Due to the distinctive structural characteristics of CB, this study showed that it has a very low reversible capacity and poor ICE when used in LIB and NIB anodes, and thus, CB cannot be utilized for LIB and

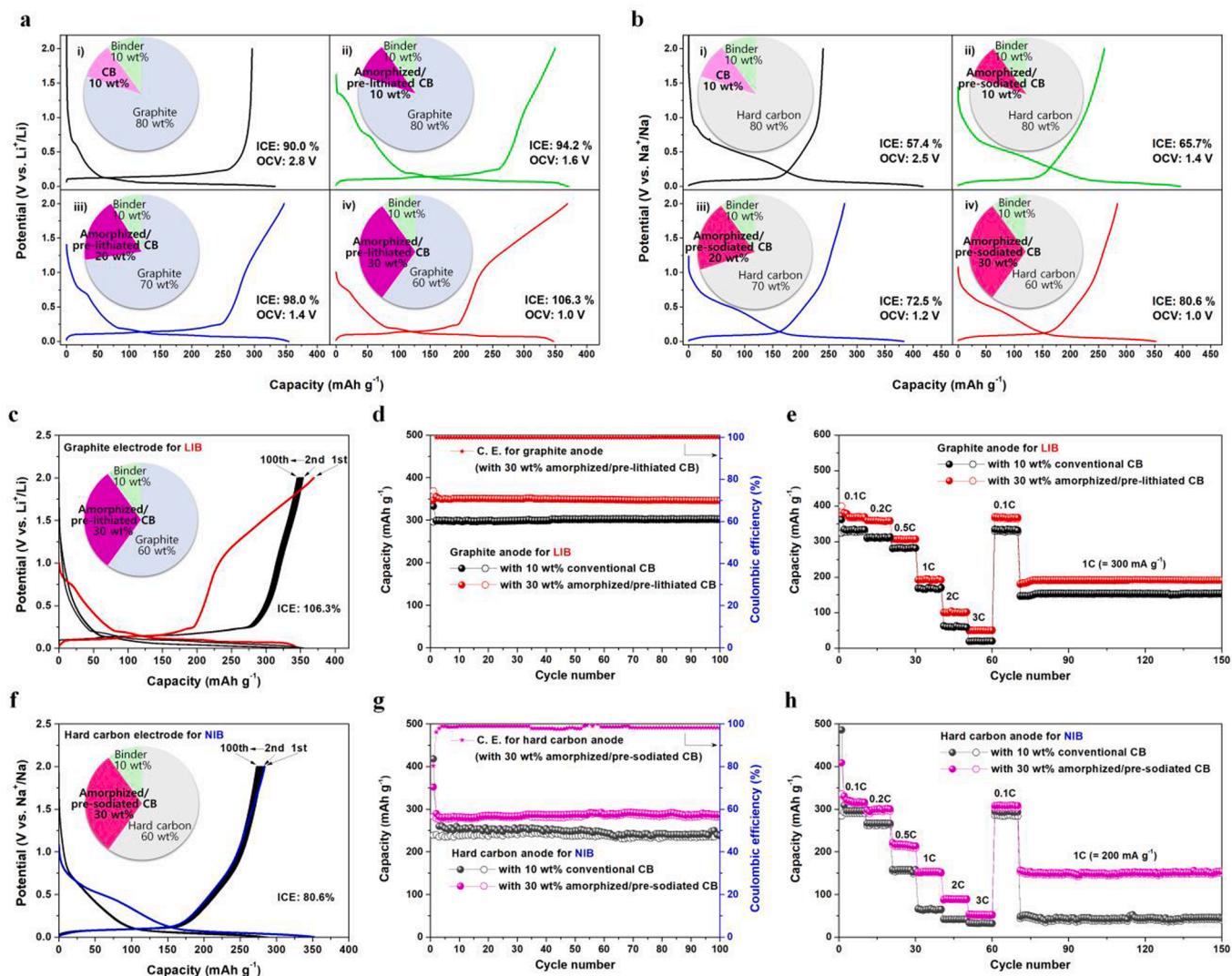


**Fig. 5.** Electrochemical performances of the amorphized/pre-lithiated and -sodiated CB as a conducting additive for LIBs and NIBs. (a) First cycle voltage profiles of graphite LIB anode (current density:  $100 \text{ mA g}^{-1}$ ) containing 10 wt% conventional CB conducting agent (i) and 10–30 wt% amorphized/pre-lithiated CB conducting additive (ii–iv). (b) First cycle voltage profiles of hard carbon NIB anode (current density:  $50 \text{ mA g}^{-1}$ ) containing 10 wt% conventional CB conducting agent (i) and 10–30 wt% amorphized/pre-sodiated CB conducting additive (ii–iv). (c) Voltage profile of graphite LIB anode containing 30 wt% amorphized/pre-lithiated CB conducting additive (current density:  $100 \text{ mA g}^{-1}$ ). (d) Cycling performances (cycling rate:  $100 \text{ mA g}^{-1}$ ), and (e) rate capabilities of graphite LIB anodes containing 30 wt% amorphized/pre-lithiated CB conducting additive (1C rate:  $300 \text{ mA g}^{-1}$ ) and containing 10 wt% conventional CB conducting agent (1C rate:  $300 \text{ mA g}^{-1}$ ). (f) Voltage profile of hard carbon NIB anode containing 30 wt% amorphized/pre-sodiated CB conducting additive (current density:  $50 \text{ mA g}^{-1}$ ). (g) Cycling performances (cycling rate:  $50 \text{ mA g}^{-1}$ ), and (h) rate capabilities of hard carbon NIB anodes containing 30 wt% amorphized/pre-sodiated CB conducting additive (1C rate:  $200 \text{ mA g}^{-1}$ ) and containing 10 wt% conventional CB conducting agent (1C rate:  $200 \text{ mA g}^{-1}$ ).

NIB systems. Therefore, a superior CB for LIBs and NIBs was successfully designed using a simple two-step strategy of amorphization and pre-lithiation/sodiation. First, the low reversible capacity of CB was increased by the generation of an increased number of Li- and Na-insertion sites by preparing amorphized CB. The amorphized CB was thoroughly analyzed using various analytical techniques; FT-IR, SEM, TEM, XRD, Raman, and C K-edge EELS analyses. Second, the poor ICE of CB was supplemented by the simple synthesis of amorphized/pre-lithiated and -sodiated CB, which involves a very simple pre-lithiation/sodiation process. The amorphized/pre-lithiated and -sodiated CB was also analyzed using various analytical techniques, including XRD, Raman, TEM, and C K-edge and Li/Na K-edge EELS. In addition, the Li- and Na-ion insertion/extraction mechanisms of CB, amorphized CB, and amorphized/pre-lithiated and -sodiated CB were fully demonstrated using the C K-edge NEXAFS analyses. As a result of the interesting reaction mechanism, the superior CB had highly reversible capacities with exceptionally high ICEs, stable reversible capacities over

100 cycles, fast rate capabilities with highly reversible capacities at fast C rates, and excellent Li- and Na-cycling behaviors of >300 cycles at a 1C rate. Notably, the superior CB can compensate ICE and increase the reversible capacity of LIB and NIB anode materials when used as a conducting additive, which is very suitable as a next generation conducting agent to replace the conventional CB. We strongly believe that the superior CB, designed using the simple two-step strategy of amorphization and pre-lithiation/sodiation, will play a major role in the anode market for LIBs and NIBs.

#### Declaration of Competing Interest

The authors declare that they have no known competing financial interests or personal relationships that could have appeared to influence the work reported in this paper.

## Acknowledgments

This work was supported by the National Research Foundation of Korea (NRF) grant, funded by the Korea Government (MSIP) (NRF-2021R1A2B5B01002570, NRF-2018R1A6A1A03025761). This research was supported by the MSIT (Ministry of Science and ICT), Korea, under the Grand Information Technology Research Center support program (IITP-2021-2020-0-01612) and supervised by the IITP (Institute for Information & Communications Technology Planning & Evaluation).

## Appendix A. Supplementary data

Supplementary data to this article can be found online at <https://doi.org/10.1016/j.cej.2021.129242>.

## References

- [1] M. Armand, J.-M. Tarascon, Building better batteries, *Nature* 451 (2008) 652–657.
- [2] N. Nitta, F. Wu, J.T. Lee, G. Yushin, Li-ion battery materials: Present and future, *Mater. Today* 18 (2015) 252–264.
- [3] N. Yabuuchi, K. Kubota, M. Dahbi, S. Komaba, Research development on sodium-ion batteries, *Chem. Rev.* 114 (2014) 11636–11682.
- [4] P. Barpanda, G. Oyama, S.-I. Nishimura, S.-C. Chung, A. Yamada, A 3.8-V earth-abundant sodium battery electrode, *Nat. Commun.* 5 (2014) 4358.
- [5] J.R. Dahn, T. Zheng, Y. Liu, J.S. Xue, Mechanisms for lithium insertion in carbonaceous materials, *Science* 270 (1995) 590–593.
- [6] M. Winter, J.O. Besenhard, M.E. Spahr, P. Novák, Insertion electrode materials for rechargeable lithium batteries, *Adv. Mater.* 10 (1998) 725–763.
- [7] P. Ge, M. Foulletier, Electrochemical intercalation of sodium in graphite, *Solid State Ionics* 28–30 (1988) 1172–1175.
- [8] D.A. Stevens, J.R. Dahn, The mechanisms of lithium and sodium insertion in carbon materials, *J. Electrochem. Soc.* 148 (2001) A803–A811.
- [9] S.W. Lee, N. Yabuuchi, B.M. Gallant, S. Chen, B.-S. Kim, P.T. Hammond, Y. Shao-Horn, High-power lithium batteries from functionalized carbon-nanotube electrodes, *Nat. Nanotechnol.* 5 (2010) 531–537.
- [10] Y.L. Cao, L.F. Xiao, M.L. Sushko, W. Wang, B. Schwenzer, J. Xiao, Z.M. Nie, L. V. Saraf, Z.G. Yang, J. Liu, Sodium ion insertion in hollow carbon nanowires for battery applications, *Nano Lett.* 12 (2012) 3783–3787.
- [11] Y.-X. Wang, S.-L. Chou, H.-K. Liu, S.-X. Dou, Reduced graphene oxide with superior cycling stability and rate capability for sodium storage, *Carbon* 57 (2013) 202–208.
- [12] Y. Wen, K. He, Y. Zhu, F. Han, Y. Xu, I. Matsuda, Y. Ishii, J. Cumings, C. Wang, Expanded graphite as superior anode for sodium-ion batteries, *Nat. Commun.* 5 (2014) 4358.
- [13] M.N. Obrovac, V.L. Chevrier, Alloy negative electrodes for Li-ion batteries, *Chem. Rev.* 114 (2014) 11444–11502.
- [14] C.-M. Park, J.-H. Kim, H. Kim, H.-J. Sohn, Li-alloy based anode materials for Li secondary batteries, *Chem. Soc. Rev.* 39 (2010) 3115–3141.
- [15] V.L. Chevrier, G. Ceder, Challenges for Na-ion negative electrodes, *J. Electrochem. Soc.* 158 (2011) A1011–A1014.
- [16] W. Luo, F. Shen, C. Bommer, H. Zhu, X. Ji, L. Hu, Na-ion battery anodes: materials and electrochemistry, *Acc. Chem. Res.* 49 (2016) 231–240.
- [17] G. Zheng, S.W. Lee, Z. Liang, H.-W. Lee, K. Yan, H. Yao, H. Wang, W. Li, S. Chu, Y. Cui, Interconnected hollow carbon nanospheres for stable lithium metal anodes, *Nat. Nanotechnol.* 9 (2014) 618–623.
- [18] J.-B. Donnet, R.C. Bansal, M.-J. Wang, *Carbon Black: Science and Technology*, Marcel Dekker, New York, 1993.
- [19] R. Dominko, M. Gaberscek, J. Drofenik, M. Bele, S. Pejovnik, J. Jamnik, The role of carbon black distribution in cathodes for Li ion batteries, *J. Power Sources* 119–121 (2003) 770–773.
- [20] L. Fransson, T. Eriksson, K. Edström, T. Gustafsson, J. Thomas, Influence of carbon black and binder on Li-ion batteries, *J. Power Sources* 101 (2001) 1–9.
- [21] K.A. See, M.A. Lumley, G.D. Stucky, C.P. Grey, R. Seshadri, Reversible capacity of conductive carbon additives at low potentials: caveats for testing alternative anode materials for Li-ion batteries, *J. Electrochem. Soc.* 164 (2016) A327–A333.
- [22] R. Gnanamuthu, C.W. Lee, Electrochemical properties of Super P carbon black as an anode active material for lithium-ion batteries, *Mater. Chem. Phys.* 130 (2011) 831–834.
- [23] C.-M. Wu, P.-I. Pan, Y.-W. Cheng, C.-P. Liu, C.-C. Chang, M. Avdeev, S. Lin, The mechanism of the sodiation and desodiation in Super P carbon electrode for sodium-ion battery, *J. Power Sources* 340 (2017) 14–21.
- [24] W. Xiao, Q. Sun, J. Liu, B. Xiao, P.-A. Glans, J. Li, R. Li, J. Guo, W. Yang, T.-K. Sham, Utilizing the full capacity of carbon black as anode for Na-ion batteries via solvent co-intercalation, *Nano Res.* 10 (2017) 4378–4387.
- [25] V. Sahu, S. Shekhar, P. Ahuja, G. Gupta, S.K. Singh, A.K. Sharma, G. Singh, Synthesis of hydrophilic carbon black; role of hydrophilicity in maintaining the hydration level and protonic conduction, *RSC Adv.* 3 (2013) 3917–3924.
- [26] J.H. Park, G. Choppala, S.J. Lee, N. Bolan, J.W. Chung, M. Edraki, Comparative sorption of Pb and Cd by biochars and its implication for metal immobilization in soils, *Water Air Soil Poll.* 224 (2013) 1711–1722.
- [27] K. Yao, Z. Xu, J. Huang, M. Ma, L. Fu, X. Shen, J. Li, M. Fu, Bundled defect-rich MoS<sub>2</sub> for a high-rate and long-life sodium-ion battery: Achieving 3D diffusion of sodium ion by vacancies to improve kinetics, *Small* 15 (2019) 1805405.
- [28] T. Enoki, M. Suzuki, M. Endo, *Graphite Intercalation Compounds and Applications*, Oxford University Press, London, 2003.
- [29] B.M. Kincaid, A.E. Meixner, P.M. Platzman, Carbon K-edge in graphite measured using electron-energy-loss spectroscopy, *Phys. Rev. Lett.* 40 (1978) 1296–1299.
- [30] L. Ponsonnet, C. Donnet, K. Varlot, J.M. Martin, A. Grill, V. Patel, EELS analysis of hydrogenated diamond-like carbon films, *Thin Solid Films* 319 (1998) 97–100.
- [31] A. Hightower, C.C. Ahn, B. Fultz, P. Rez, Electron energy-loss spectroscopy on lithiated graphite, *Appl. Phys. Lett.* 77 (2000) 238–240.
- [32] C. Suryanarayana, Mechanical alloying and milling, *Prog. Mater. Sci.* 46 (2001) 1–184.
- [33] K. Yao, Z. Xu, M. Ma, J. Li, F. Lu, J. Huang, Densified metallic MoS<sub>2</sub>/graphene enabling fast potassium-ion storage with superior gravimetric and volumetric capacities, *Adv. Funct. Mater.* 30 (2020) 2001484.
- [34] F. Nanni, G. Ruscito, D. Puglia, A. Terenzi, J. Kenny, G. Gusmano, Effect of carbon black nanoparticle intrinsic properties on the self-monitoring performance of glass fibre reinforced composite rods, *Compos. Sci. Technol.* 71 (2011) 1–8.
- [35] J. Zhao, Z. Lu, N. Liu, H.-W. Lee, M.T. McDowell, Y. Cui, Dry-air-stable lithium silicide–lithium oxide core–shell nanoparticles as high-capacity prelithiation reagents, *Nat. Commun.* 5 (2014) 5088.
- [36] X. Fan, J. Shao, X. Xiao, X. Wang, S. Li, H. Ge, L. Chen, SnLi<sub>4.4</sub> nanoparticles encapsulated in carbon matrix as high performance anode material for lithium-ion batteries, *Nano Energy* 9 (2014) 196–203.
- [37] J. Zhao, Z. Lu, H. Wang, W. Liu, H.-W. Lee, K. Yan, D. Zhuo, D. Lin, N. Liu, Y. Cui, Artificial solid electrolyte interphase-protected Li<sub>x</sub>Si nanoparticles: an efficient and stable prelithiation reagent for lithium-ion batteries, *J. Am. Chem. Soc.* 137 (2015) 8372–8375.
- [38] M.W. Forney, M.J. Ganter, J.W. Staub, R.D. Ridgley, B.J. Landi, Prelithiation of silicon–carbon nanotube anodes for lithium ion batteries by stabilized lithium metal powder (SLMP), *Nano Lett.* 13 (2013) 4158–4163.
- [39] Z. Wang, Y. Fu, Z. Zhang, S. Yuan, K. Amine, V. Battaglia, G. Liu, Application of stabilized lithium metal powder (SLMP®) in graphite anode – A high efficient prelithiation method for lithium-ion batteries, *J. Power Sources* 260 (2014) 57–61.
- [40] H.J. Kim, S. Choi, S.J. Lee, M.W. Seo, J.G. Lee, E. Deniz, Y.J. Lee, E.K. Kim, J. W. Choi, Controlled prelithiation of silicon monoxide for high performance lithium-ion rechargeable full cells, *Nano Lett.* 16 (2015) 282–288.
- [41] E. Pollak, B. Geng, K.-J. Jeon, I.T. Lucas, T.J. Richardson, F. Wang, R. Kostecki, The interaction of Li<sup>+</sup> with single-layer and few-layer graphene, *Nano Lett.* 10 (2010) 3386–3388.
- [42] F. Wang, J. Graetz, M. Sergio Moreno, C. Ma, L. Wu, V. Volkov, Y. Zhu, Chemical distribution and bonding of lithium in intercalated graphite: identification with optimized electron energy loss spectroscopy, *ACS Nano* 5 (2011) 1190–1197.
- [43] L. Zhang, X. Li, A. Augustsson, C.M. Lee, J.E. Rubensson, J. Nordgren, P.N. Ross, J. H. Guo, Revealing the electronic structure of LiC<sub>6</sub> by soft X-ray spectroscopy, *Appl. Phys. Lett.* 110 (2017), 104106.